

Spark plasma-sintered Sn-based intermetallic alloys and their Li-storage studies

P. Nithyadharseni^{1,2} · M. V. Reddy^{1,3} · B. Nalini⁴ · P. Saravanan⁵ · V. T. P. Vinod⁶ · Miroslav Černík⁶ · B. V. R. Chowdari¹

Received: 24 August 2015 / Revised: 5 March 2016 / Accepted: 17 March 2016 / Published online: 30 March 2016
© Springer-Verlag Berlin Heidelberg 2016

Abstract In the present study, SnSb, SnSb/Fe, SnSb/Co, and SnSb/Ni alloy powders processed by co-precipitation were subjected to spark plasma-sintering (SPS) at 400 °C for 5 min. The compacts were structurally and morphologically characterized by X-ray powder diffraction and scanning electron microscopy, respectively, while the electrochemical performance was investigated by galvanostatic cycling, cyclic voltammetry, and electrochemical impedance spectroscopy. Galvanostatic charge–discharge cycling of materials was examined in a voltage window of 0.005–1.5 V, with the current density of 60 mA g⁻¹. The SPSed SnSb/Fe, SnSb/Co, and SnSb/Ni compounds showed high capacities of 715, 670, 740 mAh g⁻¹ in the initial cycles. However, rapid capacity fading was observed except for

the SnSb and SnSb/Co alloy. Whereas, the SPSed SnSb alloy exhibits low reversible capacity of 528 mAh g⁻¹, but it maintained high capacity retention with good cycling stability. However, SnSb/Co alloy shows high capacity of 447 mAh g⁻¹ (capacity retention of 67 %) at the end of the 50th cycle. The result of the present study reveals that the SPSed samples exhibited good capacity retention with cycling as compared to the bulk samples obtained by other methods.

Keywords Anodes · Intermetallic alloys · Spark plasma sintering · electrochemical properties · Li-ion batteries

Introduction

The difficulty in meeting the commercial demands of lithium ion batteries is growing day by day due to the increased popularization of gadgets. Though, the limitations of carbonaceous anodes have been completely overcome by the use of various metal-based anodes such as Sn, Sb, and Si due to their high theoretical capacity (Li₂₂Si₅ 4200 mAh g⁻¹, Li₂₂Sn₅ 994 mAh g⁻¹, and Li₃Sb 660 mAh g⁻¹) [1–4]. However, these compounds have not been commercialized due to its volume change during alloying and dealloying reaction which can cause mechanical pulverization of the electrode resulting in poor cyclability. In order to overcome this problem, the intermetallic alloys [5–10] and inactive/active composite [11–15] materials, have been widely studied. Wang et al. reported that ultrafine SnSb particles prepared by hydrogen plasma–metal reaction exhibit low capacity retention of 81 % after 20 cycles [16]. Wang et al. reported that Sn₂Sb alloys synthesized by carbothermal reduction in an inert atmosphere show low capacity of 200 mAh g⁻¹ at the end of the 50th cycle [3]. Nanosized SnSb and Sn/SnSb synthesized by reductive coprecipitation shows a very low capacity of around

✉ M. V. Reddy
phymvvr@nus.edu.sg

✉ B. V. R. Chowdari
phychowd@nus.edu.sg

¹ Department of Physics, National University of Singapore, Singapore 117542, Singapore

² Energy Materials, Materials Science and Manufacturing (MSM), Council for Scientific and Industrial Research (CSIR), Pretoria 0001, South Africa

³ Department of Materials Science and Engineering, National University of Singapore, Singapore 117542, Singapore

⁴ Department of Physics, Avinashilingam institute for home science and higher education for women university, Coimbatore 641043, India

⁵ Defence Metallurgical Research Laboratory, Hyderabad 500058, India

⁶ Department of Natural Sciences, Institute for Nanomaterials, Advanced Technologies and Innovation, Technical University of Liberec, Studentská 1402/2, 46117 Liberec 1, Czech Republic

200 mAh g⁻¹ in the initial cycles for 20 % of carbon additive and for 50 % carbon additives, it shows around 400 mAh g⁻¹ at the initial cycles [17]. Sn/SnSb anode materials prepared by chemical co-precipitation method, and the final product annealed at 200 °C in air atmosphere, show very low capacity of below 200 mAh g⁻¹ obtained at the end of the 30th cycle [18]. The annealed sample shows higher impurity ratios of SnO. In order to decrease the impurity content as well as to increase the capacity and to obtain more densification of the compound, herein, we exploit the advantages of spark plasma sintering (SPS) technique. Moreover, the Sn-based alloys still demonstrate prospective grain boundary-intruded difficulties such as decreased conductivity and fractals on grain boundary due to thermal mismatch during conventional sintering. In this context, SPS has been proven to be a good alternative for avoiding such grain boundary problems in many of the solid-phase materials.

Hence, the SnSb, SnSb/Fe, SnSb/Co, and SnSb/Ni intermetallic alloys were prepared by reductive coprecipitation and the final product was SPSed at 400 °C for 5 min. By employing SPS, it is possible to consolidate the SnSb-based nanometric powders with more densification accompanied by little grain growth, and thereby high capacity with good cycling performance can be expected.

Experimental procedure

The SnSb, SnSb/Fe, SnSb/Co, and SnSb/Ni intermetallic alloys were prepared by reductive coprecipitation method, as detailed in our previous paper [11, 19]. In brief, two aqueous solutions were prepared with appropriate gram molecular weights for the synthesis of SnSb powder, namely solution 1 formed by SnCl₂·2H₂O, SbCl₃·H₂O, and sodium citrates and solution 2 constituted of NaOH and NaBH₄ (all the chemicals were of AR grade—Merck). The two solutions were mixed together to obtain the required concentration of the SnSb alloy. The precipitates thus obtained were filtered and subsequently washed with distilled water, 0.35 M HCl, and acetone until chlorine was completely washed off and dried at ambient temperature. For the preparation of Fe, Co, and Ni added SnSb alloy, the elements (Fe, Co and Ni) were substituted in excess by 1 g molecular weight of the FeCl₄, CoCl₂, and NiCl₂ in solution 1 and the reductive precipitation was carried out similar to the procedure stated above resulting in the respective SnSb alloys.

For the consolidation of SPSed SnSb, SnSb/Fe, SnSb/Co, and SnSb/Ni alloy powders, SPS 515S apparatus (Izumi Technology, Japan) was employed. The powder was placed in a graphite die (15-mm diameter) and sintered at 400 °C for 5 min. Initially, the SPS system was evacuated to 7 Pa and an electric current of ca. 400A. The diameter and thickness of the pellets are 8 and nearly 1–3 mm, respectively.

The structure of the samples was examined by X-ray powder diffraction (XRD) ($\lambda = 1.54 \text{ \AA}$, Philips X'PERT MPD unit, PANalytical) using Cu-K α radiation source. Morphology of the sample was examined by scanning electron microscopy (SEM) (JEOL-JSM 6390). More details on slurry/electrode preparation and battery fabrication are reported elsewhere [20–22]. The fabricated batteries were electrochemically evaluated by cyclic voltammetry (CV) using computer-controlled Mac-pile II system (Bio-logic, France) at the scan rate of 0.058 mV s⁻¹ and by galvanostatic cycling (GC) using Bitrode battery tester (model SCN, Bitrode, USA), at a constant current density of 60 mA g⁻¹. The batteries were tested by CV and GC in the potential ranges of 0.005–1.5 V vs. Li. The electrochemical impedance spectroscopy was carried out using Solartron/Gain phase analyzer (model SI 1255), and the plots were recorded by applying 10 mV amplitude over the frequency range from 180 kHz to 3 mHz at room temperature and the data was analysed by Z-view software (version 2.2, Scribner Assoc., Inc., USA).

Results and discussions

The XRD patterns of SPSed SnSb, SnSb/Fe, SnSb/Co, and SnSb/Ni intermetallic alloys are shown in Fig. 1. The diffraction peaks of all the compounds are assigned to the rhombohedral structure of β -SnSb phase (JCPDS no. 33–0118) with a space group of $R\bar{3}m$, 166 [11, 19]. Though, the XRD pattern of SnSb/Fe showed a small shift in the SnSb peaks, the rhombohedral structure of the compounds is not altered due to the addition of additives such as Fe, Co, and Ni. All the compounds showed some impurities; SnSb and SnSb/Ni exhibited more impurities than the other two compounds. Figure 2 shows the SEM images of SPSed SnSb, SnSb/Fe, SnSb/Co, and SnSb/Ni intermetallic alloys. The SEM images of the SnSb alloy shows more agglomerated particles than the other three samples. However, it should be

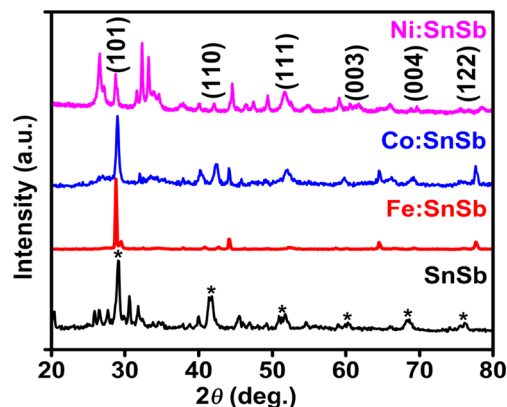
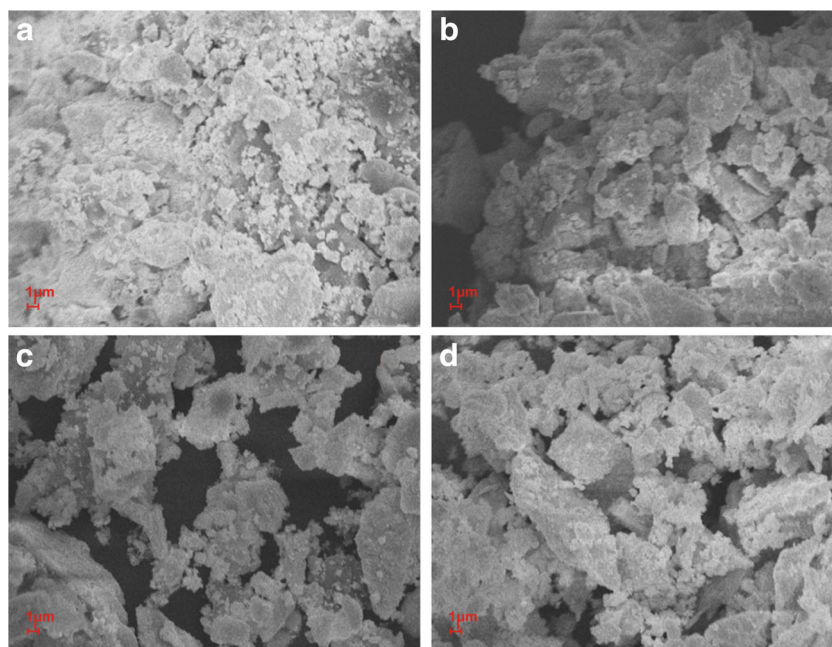


Fig. 1 XRD patterns of SPSed SnSb, SnSb/Fe, SnSb/Co, and SnSb/Ni alloys

Fig. 2 SEM images of SPSed SnSb (a), SnSb/Fe (b), SnSb/Co (c), and SnSb/Ni (d) intermetallic alloys



noted that the agglomerates essentially consist of individual fine particles or small grains.

Galvanostatic cycling performance of discharge and charge curves of SPSed SnSb, SnSb/Fe, SnSb/Co, and SnSb/Ni intermetallic alloys are shown in Fig. 3a–d. All the samples were cycled in the range of 0.005–1.5 V versus Li with the constant current density at 60 mA g⁻¹. In the first cycle of all the compounds, there is a plateau at around 1.4 V which belongs to the solid electrolyte interface (SEI) film formation [5]. From the second cycle onwards, the peak at 1.4 V disappeared and a new peak rose at around 0.9 V, corresponding to the

Li₃Sb alloy formation, and the peak at around 0.25 V belongs to various Sn alloying formation with Li. The first cycle discharge capacity of all the intermetallic alloys are 946, 1495, 1440, and 1435 mAh g⁻¹. Compared to the SnSb alloy, the Fe, Co, and Ni added SnSb alloys show high initial irreversible capacity loss. However, the initial irreversible capacity (ICL) loss was very low as compared to the other reported alloys prepared by conventional methods such as coprecipitation [5, 7, 11, 23–27], and the comparative literature data are given in Table 1. The less ICL might be due to the large particle size of the compounds; usually, smaller particles are expected to have

Fig. 3 Galvanostatic discharge–charge cycle of SPSed SnSb (a), SnSb/Fe (b), SnSb/Co (c), and SnSb/Ni (d) intermetallic alloys at the voltage range of 0.005–1.5 V and current density 60 mA g⁻¹

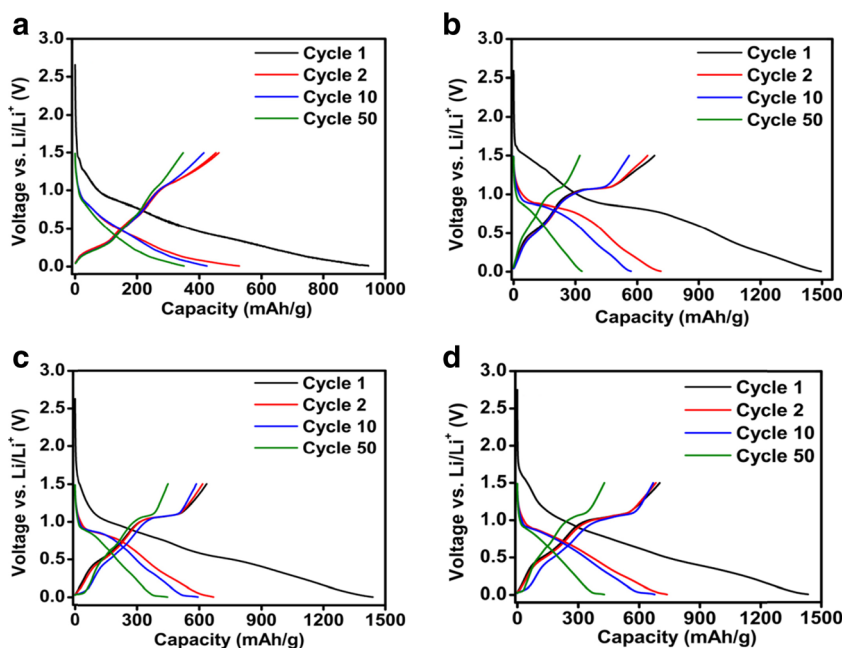


Table 1 Comparative literature data with our present work on SnSb based alloys - Discharge capacity (DC), Initial irreversible capacity loss (ICL), Coulombic efficiency (CE) and Current density (CD)

| Compound name | 1st cycle DC ($\pm 10 \text{ mAh g}^{-1}$) | 2nd cycle DC ($\pm 10 \text{ mAh g}^{-1}$) | ICL (mAh g^{-1}) | 1st CE (%) | 20th DC ($\pm 10 \text{ mAh g}^{-1}$) | 50th DC ($\pm 10 \text{ mAh g}^{-1}$) | CD (mA g^{-1}) |
|------------------------|----------------------------------------------|----------------------------------------------|-----------------------------|------------|-----------------------------------------|-----------------------------------------|---------------------------|
| SnSb (ref. [23]) | 1173 | 700 | 473 | 59 | 500 | – | 50 |
| SnSb (ref. [24]) | 1200 | 800 | 400 | 60 | 600 | – | 50 |
| SnSb/C (ref. [25]) | 900 | 400 | 500 | – | – | 350 | 50 |
| SnSb (27) | 1350 | 900 | 450 | – | – | – | 50 |
| SnSb | 1500 | 900 | 600 | 60 | 10 | – | 80 |
| SnSb-GNS | 1900 | 1200 | 700 | 63 | – | – | – |
| SnSb-GNS@C (ref. [26]) | 1500 | 1100 | 400 | – | – | – | – |
| SnSb (ref. [5]) | 1500 | 550 | 950 | 37 | – | 300 | 60 |
| SnSb | 1550 | 700 | 850 | 45 | – | 330 | 60 |
| SnSb-CNT | 1600 | 800 | 800 | 50 | – | 400 | – |
| Si-SnSb | 2450 | 1200 | 1250 | 49 | – | 450 | – |
| Si-SnSb-CNT (ref. [7]) | 1800 | 900 | 900 | 50 | – | 480 | – |
| SnSb/Fe | 1680 | 800 | 880 | 48 | – | 530 | 60 |
| SnSb/Co | 2630 | 1200 | 1430 | 46 | – | 580 | – |
| SnSb/Ni (ref. [11]) | 1565 | 900 | 665 | 58 | – | 470 | – |
| SnSb | 950 | 550 | 400 | 62 | – | 351 | 60 |
| SnSb/Fe | 1500 | 700 | 800 | 47 | – | 331 | – |
| SnSb/Co | 1450 | 650 | 800 | 45 | – | 447 | – |
| SnSb/Ni (Present work) | 1430 | 720 | 710 | 50 | – | 428 | – |

high ICL. The ICL could be due to the decomposition of the solvent in the electrolyte which causes SEI formation on the surface of the electrode, crystal structure, and voltage range of cycling [1]. The reversible capacity fading is much less for SnSb and SnSb/Co alloys; meanwhile, the reversible capacity fading is very high for the SnSb/Fe and SnSb/Ni alloys from

the second cycle to the end of the 50th cycle. Compared to the literature [19], the samples SPSeD at 400 °C demonstrated high capacity retention with good cycling behavior.

Cycling performance of SnSb, SnSb/Fe, SnSb/Co, and SnSb/Ni intermetallic alloys are shown in Fig 4a–d. The overall reversible capacities of the intermetallic alloys are 351,

Fig. 4 Cycle number versus capacity plots of SPSeD SnSb (a), SnSb/Fe (b), SnSb/Co (c), and SnSb/Ni (d) intermetallic alloys, at voltage range of 0.005–1.5 V and current density of 60 mA g^{-1}

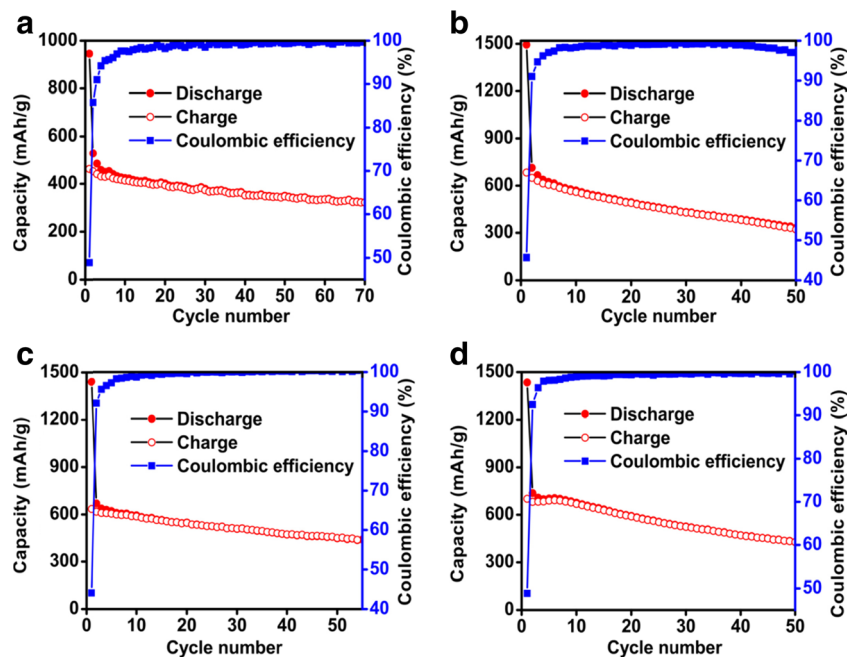
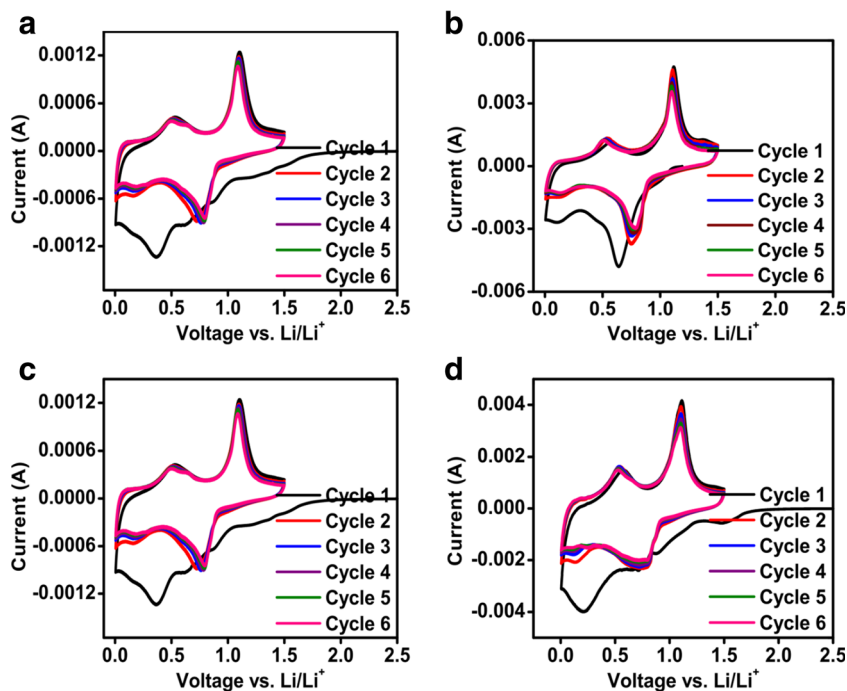


Fig. 5 Cyclic voltammogram of SPSed SnSb (a), SnSb/Fe (b), SnSb/Co (c), and SnSb/Ni (d) intermetallic alloys; scan rate 0.058 mV s⁻¹ and voltage window 0.005–1.5 V versus Li



331, 447, and 428 mAh g⁻¹, respectively, at the end of 50th cycle. The capacity retention for all the compounds is 66.5, 46, 67, and 58 % after 50 cycles. The SnSb and SnSb/Co alloys show minimal capacity fading compared to SnSb/Fe and SnSb/Ni alloys. The SnSb/Fe shows more capacity fading than the all other intermetallic alloys. However, SnSb/Ni shows low capacity fading from second cycle to tenth cycle and afterwards, the rapid capacity fading was observed until 50th cycle. The decrease in capacity fading in the initial cycles might be due to the inactive matrix of Ni, which can easily buffer the volume change during cycling process [12, 13]. Even though, the SnSb/Co shows high capacity retention than the all other three compounds. However, the capacity value is very low compared to our previous results but the cycling stability was improved by SPS technique [11]. Compared to the previous literature [14, 25, 26, 28, 29], our SPSed samples exhibit high capacity with good retention and better cycling performance. Though in all the compounds, the capacity decay is observed upon cycling which could be associated to the binder (PVDF). Indeed, it must be discussed, that the binder may play a crucial role in influencing the performance of high-volume change of electrode materials.

Figure 5a–d shows cyclic voltammetry of SPSed SnSb, SnSb/Fe, SnSb/Co, and SnSb/Ni intermetallic alloys cycled

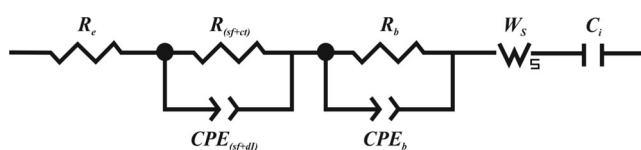


Fig. 6 Equivalent electrical circuit for all the samples

in the range of 0.005–1.5 V at a scan rate of 0.058 mV s⁻¹. The first cycle of all the compounds shows a peak at around 1.0 V corresponding to the SEI film formation. From the second cycle onwards, the peak at 1.0 V disappeared for all the compounds, which indicates that the SEI formation only occurs in the first cycle. From 2 to 6 cycles, the peak at around 0.8 V belongs to the alloying formation of Sb to Li (Li₃Sb) [30, 31]. Then, the other peak at around 0.55 V corresponding to the Sn–Li formation and the peak at 0.3 V belongs to various Sn alloying formation with Li (Li_xSn) [32]. For all the compounds the anodic peaks around ~1.1 and 0.6 V can be noticed, attributed to the dealloying process of Li–Sb and Li–Sn.

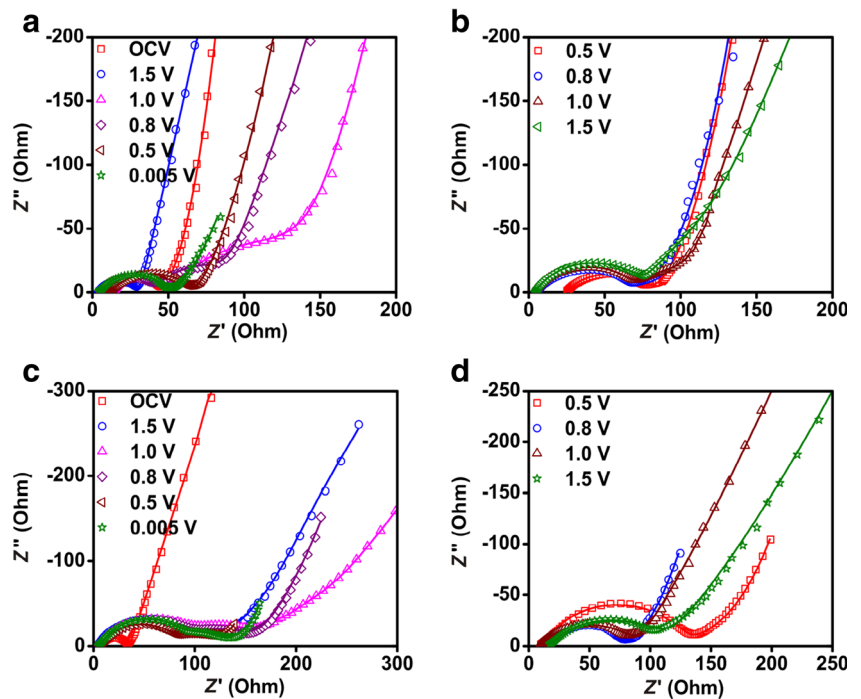
Electrochemical impedance spectroscopy (EIS) was carried out for SPSed SnSb, SnSb/Fe, SnSb/Co, and SnSb/Ni intermetallic alloys in order to investigate the kinetic properties of Li⁺ ions of the anode materials. The impedance spectra was examined for the fresh cell (open circuit voltage (OCV)) and during the first charge and discharge states at different voltages (charge at 0.5, 0.8, 1.0, 1.5 V and discharge at 1.5, 1.0, 0.8, 0.5, 0.005 V vs. Li) with the current density of 60 mA g⁻¹. The data were plotted as Nyquist plots (*Z'* vs. *-Z''*) and are fitted by using an equivalent circuit as shown in Fig. 6. The equivalent circuit consists of resistance (which contributes to electrolyte, surface film (*sf*), charge transfer (*ct*), and bulk resistance (*b*)), constant phase element (donates to *sf*, double layer (*dl*), and constant phase element was used instead of pure capacitor due to the composite nature of the electrode), Warburg impedance (*W_s*) and intercalation capacitance (*C_i*) [33]. The fitted impedance parameters are listed in Table 2.

Figure 7a–d and Fig. 8a–d shows Nyquist plots of SPSed SnSb, SnSb/Fe, SnSb/Co, and SnSb/Ni intermetallic alloys

Table 2 Fitted impedance values of SPSe_d SnSb, SnSb/Fe, SnSb/Co, and SnSb/Ni intermetallic alloys using equivalent electrical circuit

| Voltage | $R_{(sf+ct)}$ ($\pm 5 \Omega$) | $CPE_{(sf+dl)}$ ($\pm 3 \mu\text{F}$) | α (± 0.02) | R_b ($\pm 3 \Omega$) | CPE_b ($\pm 3 \text{mF}$) | α (± 0.02) | W_s ($\pm 10 \Omega$) | C_i (F) |
|---------------------------------|----------------------------------|-----------------------------------------|-------------------------|--------------------------|-------------------------------|-------------------------|---------------------------|-----------|
| SnSb (first discharge cycle) | | | | | | | | |
| 2.8 V (OCV) | 38 | 25 | 0.65 | – | – | – | 553 | 0.01 |
| 1.5 V | 27 | 18 | 0.64 | – | – | – | 811 | 0.03 |
| 1.0 V | 39 | 21 | 0.69 | 90 | 32 | – | 655 | 0.08 |
| 0.8 V | 40 | 22 | 0.65 | 41 | 21 | – | 724 | 0.19 |
| 0.5 V | 56 | 27 | 0.59 | – | – | – | 561 | 0.11 |
| 0.005 V | 44 | 24 | 0.67 | – | – | – | 248 | 0.72 |
| First charge cycle | | | | | | | | |
| 0.5 V | 56 | 26 | 0.58 | – | – | – | 572 | 0.09 |
| 0.8 V | 66 | 31 | 0.60 | – | – | – | 585 | 0.07 |
| 1.0 V | 67 | 31 | 0.65 | 34 | 22 | – | 1165 | 0.26 |
| 1.5 V | 64 | 30 | 0.70 | – | – | – | 853 | 0.01 |
| SnSb/Fe (first discharge cycle) | | | | | | | | |
| 2.8 V (OCV) | 30 | 20 | 0.72 | – | – | – | 673 | 0.36 |
| 1.5 V | 115 | 22 | 0.60 | – | – | – | 180 | 0.10 |
| 1.0 V | 59 | 28 | 0.79 | 111 | 18 | – | 225 | 0.02 |
| 0.8 V | 88 | 25 | 0.69 | 59 | 11 | – | 636 | 0.09 |
| 0.5 V | 66 | 29 | 0.73 | 23 | 06 | – | 538 | 0.55 |
| 0.005 V | 81 | 27 | 0.77 | 24 | 07 | – | 356 | 0.14 |
| First charge cycle | | | | | | | | |
| 0.5 V | 122 | 32 | 0.65 | – | – | – | 538 | 0.01 |
| 0.8 V | 66 | 28 | 0.67 | – | – | – | 898 | 0.89 |
| 1.0 V | 70 | 29 | 0.63 | – | – | – | 696 | 0.63 |
| 1.5 V | 93 | 30 | 0.68 | – | – | – | 674 | 0.42 |
| SnSb/Co (first discharge cycle) | | | | | | | | |
| 2.8 V (OCV) | 33 | 21 | 0.72 | – | – | – | 228 | 0.02 |
| 1.5 V | 32 | 22 | 0.75 | – | – | – | 261 | 0.01 |
| 1.0 V | 41 | 24 | 0.69 | 81 | 32 | – | 292 | 0.19 |
| 0.8 V | 43 | 25 | 0.69 | 32 | 21 | – | 722 | 0.05 |
| 0.5 V | 55 | 29 | 0.69 | 13 | 09 | – | 548 | 0.39 |
| 0.005 V | 54 | 27 | 0.70 | 14 | 10 | – | 335 | 0.51 |
| First charge cycle | | | | | | | | |
| 0.5 V | 52 | 29 | 0.65 | – | – | – | 148 | 0.05 |
| 0.8 V | 44 | 26 | 0.67 | – | – | – | 276 | 0.45 |
| 1.0 V | 39 | 23 | 0.63 | – | – | – | 510 | 0.52 |
| 1.5 V | 52 | 27 | 0.68 | – | – | – | 529 | 0.63 |
| SnSb/Ni (first discharge cycle) | | | | | | | | |
| 2.8 V (OCV) | 50 | 28 | 0.66 | – | – | – | 484 | 0.02 |
| 1.5 V | 35 | 21 | 0.69 | – | – | – | 190 | 1.23 |
| 1.0 V | 55 | 29 | 0.71 | – | – | – | 580 | 0.03 |
| 0.8 V | 63 | 30 | 0.68 | – | – | – | 272 | 0.04 |
| 0.5 V | 70 | 32 | 0.69 | – | – | – | 322 | 0.01 |
| 0.005 V | 42 | 23 | 0.68 | – | – | – | 345 | 0.01 |
| First charge cycle | | | | | | | | |
| 0.5 | 56 | 28 | 0.69 | – | – | – | 669 | 0.02 |
| 0.8 | 85 | 31 | 0.72 | – | – | – | 833 | 0.01 |
| 1.0 | 93 | 32 | 0.71 | – | – | – | 743 | 0.13 |
| 1.5 | 98 | 32 | 0.72 | – | – | – | 802 | 0.01 |

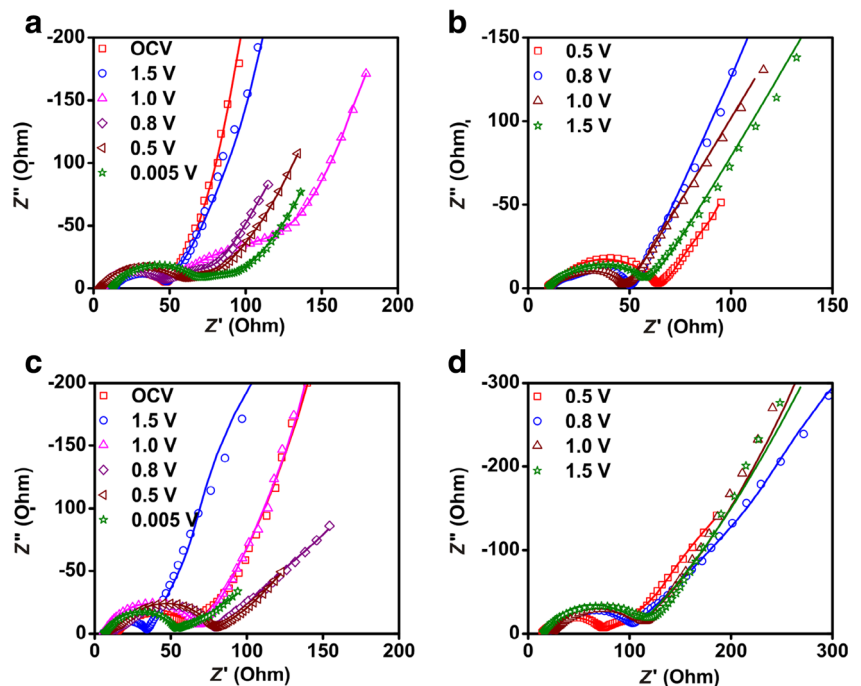
Fig. 7 Nyquist plots (Z' vs. Z'') for SPSe d SnSb, SnSb/Fe during (a, c) the first discharge and (b, d) the first charge at various voltages. Symbols represent experimental data and continuous line is fitted data



during the first discharge and charge states at different voltages. In all the graphs, the dotted line represents the experimental data and the straight line signifies its calculated data. The fresh cell (OCV \sim 2.8 V) of all the compounds shows a single semicircle in the high-mid frequency region which corresponds to the resistance that contributes to surface film and charge transfer ($R_{(sf + ct)}$) and constant phase element that contributes to the double-layer capacitance ($CPE_{(sf + dl)}$), and

the slope in the low frequency region corresponds to Warburg impedance (W_s). Figure 7a, b shows SPSe d SnSb alloys at discharge and charge states. The $R_{(sf + ct)}$ values started increasing gradually from 1.5 V to 0.5 V, then it is suddenly decreased to 44 Ω at 0.005 V during the discharge state. During charging, the resistance values started increasing due to the increasing voltage. The $CPE_{(sf + dl)}$ values are also varied corresponding to the resistance values and the voltage.

Fig. 8 Nyquist plots for SPSe d SnSb/Co, SnSb/Ni during a, c the first discharge and b, d the first charge at various voltages. Symbols represent experimental data and continuous line is fitted data



The Nyquist plot of SPSed SnSn/Fe during discharge and charge states is shown in Fig. 7b, d. During discharging from 1.0 to 0.005 V, all the impedance spectra show two semicircles, one at high frequency, the other at mid to low frequency region and they belong to $R_{(sf+ct)}$ and bulk resistance (b), respectively. The R_b rises due to electronic resistance of active material and ionic resistance of the electrolyte filled in the pores of the composite electrode [11, 34]. The α -values of SPSed SnSb and SnSb/Fe during the first discharge and charge cycle are in the range of 0.59–0.79.

Figure 8a, b shows Nyquist plot of SPSed SnSb/Co alloys at charge and discharge states. During discharge from 1.5 to 0.8 V, the resistance values started decreasing and after that, the values started increasing; meanwhile, during charging state, the resistance values are decreasing up to 1.0 V, but the values are increasing at 1.5 V. The $R_{(sf+ct)}$ and R_b values are varied from 32 to 54 Ω and 13–32 Ω for SnSb/Co samples, respectively. Figure 8c, d shows Nyquist plots of SnSb/Ni at discharge and charge states. The SnSb/Ni sample shows single semicircle for discharging and charging state. During discharging and charging, the resistance values are varied according to the voltage. The α -values during the first discharge and charge cycle of SPSed SnSb/Co and SnSb/Ni alloys are in the range of 0.63–0.75. W_s is the Warburg resistance of the compounds that is specified in Table 2, which is associated with the solid-state diffusion of Li^+ ions through the lattice of the compounds. In the Nyquist plot, most of the spectra show Warburg behavior to a capacitive behavior in the lower frequency range, which is represented by a vertical line in the complex plane representation. This observed behavior in these compounds is due to the diffusion penetration depth can reach the impermeable current collector of the center of the nanoparticles, which causes the shorter diffusion lengths in the particles. Those effects lead to effectively emptying or filling up the active material like a capacitor. This behavior in the Warburg impedance in the low frequency region is called the open circuit (blocked) diffusion [35]. This Warburg impedance diffusion is mainly related to impact of particle size and the geometry of the particle in the compound, but in our study, the compounds show agglomerated particles; on further electrochemical cycling, we can expect the differences in particle sizes. Therefore, our group is currently working on the effect of particle size related to the Warburg diffusion of the compounds. When the materials are discharged at higher voltage (1 or 1.5 V), the resistance of the compounds are increasing, which means the lithium ion diffusion are very low, but during low voltage (below 1.0 V), the charge transfer resistance are decreased, denoting that the lithium diffusion levels are moderately increasing in the compounds. Thus, it is clear that the observed impedance parameters of SPSed SnSb, SnSb/Fe, SnSb/Co, and SnSb/Ni as a function of voltage are consistent with the galvanostatic cycling data. Further careful studies on Li diffusion coefficient studies by GC, CV, and impedance

and other spectroscopy techniques are needed on variation of particle size during electrochemical cycling.

Conclusion

SnSb, SnSb/Fe, SnSb/Co, and SnSb/Ni intermetallic alloys were prepared by reductive coprecipitation method, followed by spark plasma sintering at 400 °C for 5 min. The XRD pattern of all the SPSed samples showed rhombohedral structure of β -SnSb phase, along with some minor impurities of parent materials. The discharge capacity of all the SPSed samples exhibited 351, 331, 447, and 428 mAh g^{-1} at the end of the 50th cycle. Among those, SnSb/Co showed high capacity retention of 66 % (447 mAh g^{-1}) at the end of the 50th cycle. In contrast, the SnSb alloy exhibited better cycling performance than the other three intermetallic alloys.

Acknowledgments Dr. Nithya gratefully acknowledges the National University of Singapore (NUS) for partial financial support through the NUS-India research initiative (NUS-IRI R069000006646) fund and Council for Scientific and Industrial Research (CSIR), Pretoria, South Africa. The authors V.T.P.V. and M.C. acknowledge the support rendered by the Ministry of Education, Youth and Sports under the National Programme for Sustainability I, OPR&DI project (LO1201), and OP VaVpI of the Centre for Nanomaterials, Advanced Technologies and Innovation-CZ.1.05/2.1.00/01.0005.

References

- Reddy MV, Subba Rao GV, Chowdari BVR (2013) Chem Rev 113: 5364–5457
- Jung YS, Lee KT, Oh SM (2007) Electrochim Acta 52:7061–7067
- Kasavajula U, Wang C, Appleby AJ (2007) J Power Sources 163: 1003–1039
- Wang K, He X, Ren J, Wang L, Jiang C, Wan C (2006) Electrochim Acta 52:1221–1225
- Nithyadharseni P, Reddy MV, Nalini B, Chowdari BVR (2015) Mater Lett 150:24–27
- Jishi Z, Li W, He X, Chunrong W, Changyin J (2008) Electrochim Acta 53:7048–7053
- Nithyadharseni P, Reddy MV, Nalini B, Ravindran TR, Pillai BC, Kalpana M, Chowdari BVR (2015) Mater Res Bull 70:478–485
- Rom I, Wachtler M, Papst I, Schmied M, Besenhard JO, Hofer F, Winter M (2001) Solid State Ionic 143:329–336
- Shukla AK, Prem Kumar T (2008) Current Sci 94:314–331
- Li H, Shi L, Wang Q, Chen L, Huang X (2002) Solid State Ionic 148:247–258
- Nithyadharseni P, Reddy MV, Nalini B, Kalpana M, Chowdari BVR (2015) Electrochim Acta 161:261–268
- Guo H, Lin XF, Chen YS (2010) Trans Nonferrous Met Soc China 20:s253–s256
- Guo H, Zhao H, Chaoli Y, Weihua Q (2006) J Alloy Compound 426:277–280
- Guo H, Zhao H, Jia X, He J, Qiu W, Li X (2007) J Power Source 174:921–926
- Wang F, Zhao M, Song X (2008) J Power Source 175:558–563
- Wang Z, Tian W, Li X (2007) J Alloy Compound 439:350–354

17. Needham SA, Wang GX, Liu HK (2005) *J Alloy Compound* 400: 234–238
18. Mukaibo H, Osaka T, Reale P, Panero S, Scrosati B, Wachtler M (2004) *J Power Sources* 132:225–228
19. Nithyadharseni P, Nalini B, Saravanan P (2014) *Appl Sur Sci* 311: 503–507
20. Reddy MV, Khai VH, Chowdari BVR (2015) *Mater Lett* 140:115–118
21. Nithyadharseni P, Reddy MV, Fanny H, Adams S, Chowdari BVR (2015) *RSC Adv* 6:60552–60561
22. Shaikshavali P, Srikanth VSS, Nithyadharseni P, Reddy MV, Adams S, Chowdari BVR (2015) *ACS Sustain Chem Eng* 3: 3205–3213
23. Wang Z, Tian W, Liu X, Yang R, Li X (2007) *J Solid State Chem* 180:3360–3365
24. Wang F, Zhao M, Song X (2009) *J Alloy Compound* 472:55–58
25. Hassoun J, Derrien G, Panero S, Scrosati B (2009) *Electrochim Acta* 54:4441–4444
26. Chen S, Chen P, Wu M, Pan D, Wang Y (2010) *Electrochem Commun* 12:1302–1306
27. Li Y, Zhang W, Cai H, Wang J, Ren X, Zhang P (2015) *RSC Adv* 5: 105643–105650
28. Park CM, Sohn HJ (2009) *Electrochim Acta* 54:6367–6373
29. Billaud D, Nabais C, Mercier C, Schneider R, Willmann P (2008) *Energy Convers Manag* 49:2447–2454
30. Yin C, Zhao H, Guo H, Huang X, Qiu W (2007) *J Univ Sci Tech Beijing* 14:345–349
31. Zhang SQ, Chen CH (2008) *Mater Res Bull* 43:3601–3606
32. Simonin L, Lafont U, Kelder EM (2008) *J Power Sources* 180:859–863
33. Nithyadharseni P, Reddy MV, Kenneth IO, Geetha RB, Chowdari BVR (2015) *Electrochim Acta* 182:1060–1069
34. Reddy MV, Subba Rao GV, Chowdari BVR (2011) *J Mater Chem* 21:10003–10011
35. Song J, Bazant ZM (2013) *J Electrochem Soc* 160:A15–A24